

Embedded Lensing Time Delays, the Fermat Potential, and the Integrated Sachs-Wolfe Effect

Bin Chen^{1,2}, Ronald Kantowski¹, Xinyu Dai¹

ABSTRACT

We derive the Fermat potential for a spherically symmetric lens embedded in an FLRW cosmology and use it to investigate the late-time integrated Sachs-Wolfe (ISW) effect, i.e., secondary temperature fluctuations in the cosmic microwave background (CMB) caused by individual large scale clusters and voids. We present a simple analytical expression for the temperature fluctuation in the CMB across such a lens as a derivative of the lens' Fermat potential. This formalism is applicable to both linear and nonlinear density evolution scenarios, to arbitrarily large density contrasts, and to all open and closed background cosmologies. It is much simpler to use and makes the same predictions as conventional approaches. In this approach the total temperature fluctuation can be split into a time-delay part and an evolutionary part. Both parts must be included for cosmic structures that evolve and both can be equally important. We present very simple ISW models for cosmic voids and galaxy clusters to illustrate the ease of use of our formalism. We use the Fermat potentials of simple cosmic void models to compare predicted ISW effects with those recently extracted from WMAP and *Planck* data by stacking large cosmic voids using the aperture photometry method. If voids in the local universe with large density contrasts are no longer evolving we find that the time delay contribution alone predicts values consistent with the measurements. However, we find that for voids still evolving linearly, the evolutionary contribution cancels a significant part of the time delay contribution and results in predicted signals that are much smaller than recently observed.

Subject headings: cosmic background radiation—cosmology: theory—gravitation—gravitational lensing: strong—large-scale structure of universe

¹Homer L. Dodge Department of Physics and Astronomy, University of Oklahoma, Norman, OK 73019, USA

²Research Computing Center, Department of Scientific Computing, Florida State University, Tallahassee, FL 32306, USA, bchen3@fsu.edu

1. Introduction

The cosmic microwave background (CMB) exhibits an intrinsic temperature anisotropy caused by the primordial density perturbations. Determining the spectrum of this primary anisotropy is of fundamental importance to modern cosmology. The accurate evaluation of this spectrum is complicated by the presence of *secondary* anisotropies caused by the thermo/kinetic Sunyaev-Zeldovich effect (Zeldovich & Sunyaev 1969; Sunyaev & Zeldovich 1980; Birkinshaw 1999), the integrated Sachs-Wolfe (ISW) effect (Sachs & Wolfe 1967), gravitational lensing (Cole & Efstathiou 1989; Seljak 1996a), and reionization (Vishniac 1987; Hu 2000; Miralda-Escudé et al. 2000). In this paper we are mainly interested in the ISW effect caused by inhomogeneities that exist along the line of sight from observation back to the CMB’s decoupling at around redshift $z \sim 1100$ (the last scattering surface). ISW fluctuations caused by nonlinear growths of density perturbations at low redshifts were investigated in Rees & Sciama (1968) using Swiss cheese models (Einstein & Straus 1945; Schücker 1954) and their presence is referred to as the Rees-Sciama (RS) effect. The importance of the ISW/RS effect to modern cosmology is multifold. First, studying the effect probes the evolution history of cosmic structures and the dynamics of dark energy. For example, in a flat Λ CDM universe, a nonzero cosmological constant causes the expansion of the universe to accelerate, resulting in a decay of the gravitational potentials associated with cosmic voids, and thus leaving its evolutionary imprint on the observed CMB anisotropies. Detecting this effect is considered a crucial test for the presence of dark energy, since it directly probes the negative pressure nature of dark energy and complements other methods which are geometrical in nature, e.g., using SNe Ia as standard candles (Riess et al. 1998; Perlmutter et al. 1999) or using baryonic acoustic oscillations as standard rulers (Eisenstein et al. 2005). Second, the ISW/RS effect caused by local inhomogeneities, in particular, cosmic voids, has been used extensively to explain several large angle anomalies in CMB anisotropies observed by the Wilkinson Microwave Anisotropy Probe (WMAP; Bennett et al. 2003). For example, the octopole planarity (a preferred axis along which the octopole power is suppressed), the alignment between the quadrupole and the octopole moments, the anomalously cold spot on the south hemisphere, and the temperature asymmetry in the large angle power between opposite hemispheres all have possible explanations via the ISW/RS effect (Tegmark et al. 2003; Velva et al. 2004; Cooray & Seto 2005; Inoue & Silk 2006; Rudnick et al. 2007; Szapudi et al. 2014a,b; Finelli et al. 2014; Nadathur et al. 2014). Accurately measuring the ISW/RS effect is also important for detecting possible non-Gaussian signatures in the primordial density spectrum. To measure the primordial non-Gaussianity of the initial density spectrum, *secondary* non-Gaussianities caused by the ISW/RS effect, have to be systematically investigated and removed (Kim et al. 2013). For example, the ISW-lensing bispectrum has been recently detected by *Planck* (Planck Collaboration et al. 2014a).

Even though Rees & Sciama (1968) pointed out that the time delay experienced by a CMB photon crossing a mass over-density can cause significant temperature fluctuations, the RS effect today usually refers only to those fluctuations caused by time-dependent potentials. Detailed theoretical investigation of the ISW effect continues to date (Dyer 1976; Nottale 1984; Martínez-González et al. 1990; Panek 1992; Seljak 1996b; Cooray 2002a,b; Sakai & Inoue 2008; Valkenburg 2009; Smith et al. 2009). Observational detection of the ISW effect includes the two following approaches. First by constructing the correlation function between the CMB temperature sky map and tracers of large scale structures in different wavelengths (Boughn & Crittenden 2004; Ho et al. 2008; Dupé et al. 2011), hot and cold spot directions are compared with galaxy over and under-densities. This correlation has been tentatively found by the Planck Collaboration et al. (2014b). The second approach is based on aperture photometry, i.e., patches of CMB maps around known large cosmic voids and clusters are stacked and averaged in order to minimize contamination from *primordial* anisotropies and to detect cold or hot spots due to the ISW effect. Recently several groups claimed detection of the ISW effect using this second method (Granett et al. 2008a,b; Planck Collaboration et al. 2014b), although doubts exist (Hernández-Monteagudo 2010; Nadathur et al. 2012; Ilić et al. 2013) based on linear structure growth rates in a Λ CDM universe. One major controversy surrounding the void-stacking method is the large value of the observed fluctuations compared to theoretical predictions and numerical simulations (Maturi et al. 2007; Cai et al. 2010, 2014; Nadathur et al. 2012; Ilić et al. 2013; Hernández-Monteagudo & Smith 2013; Flender et al. 2013; Watson et al. 2014; Hotchkiss et al. 2015). Another surprising result of this method is the strange shape of the photometric profile, including the hot ring in the outer part of the profile (Ilić et al. 2013; Planck Collaboration et al. 2014b). This structure is also hard to explain within the framework of the linear ISW effect in a standard Λ CDM cosmology (see Fig. 9 of Planck Collaboration et al. 2014b).

Here we present a theory which is easy to use and which may help to resolve these differences. We investigate the effect of lensing by individual large scale structures on observed CMB temperature fluctuations using our recently developed embedded lens theory (Kantowski et al. 2010, 2012, 2013, 2014; Chen et al. 2010, 2011, 2015). Our lens is the same as a general Swiss cheese condensation but so named to emphasize the consequences of embedding, i.e., the consequences of making the lens mass a contributor to the mean mass density of the universe. An embedded lens is constructed by first removing a comoving sphere from a homogeneous Friedman-Lemaître-Robertson-Walker (FLRW) universe, producing a vacuole, or a Swiss cheese void, then deforming that mass into an arbitrary spherical shape, and placing it back into the void in such a way as to keep Einstein’s equations satisfied

throughout (Einstein & Straus 1945; Schücking 1954).¹ Deformed mass densities can be over-dense in the central region and represent galaxy clusters or under-dense in the central region and represent cosmic voids. Because of general relativity's (GR) boundary conditions the average density throughout the refilled Swiss cheese void is essentially the same as the background cosmology. Consequently the dense central region of an embedded cluster lens model must be surrounded by an under-dense (void like) region (see Fig. 1). For the same reason an embedded lens model for a cosmic void which is low in central mass density must be surrounded by an over-dense region (often a shell of mass). By using the embedded lens model and satisfying Einstein's equations we are assured that gravitational approximation errors are not inherent at any order. Until now most analytical expressions for temperature fluctuations in the CMB caused by crossing individual cosmic structures have been complicated and were best presented in graphical form. By keeping only the lowest order lensing terms and using the Fermat potential we are able to give a simple analytical expression for such fluctuations.

In Section 2 we present the fundamental theoretical result of this paper, Eq. (5), a simple relation between the Fermat potential and the ISW effect. In Section 3 we apply this theory to two simple embedded lens models, one for linearly growing structures and one for co-expanding structures. For simplicity we assume the clusters have stopped evolving relative to the background cosmology but for the voids we additionally compute an evolutionary correction by assuming the voids are still evolving linearly. Conclusions are drawn in Section 4. In Appendix A we present a subtle derivation of Eq. (5). In Appendix B we check the validity of Eq. (5) by comparing its prediction for the embedded point mass lens with the prediction made by the conventional approach.

2. The Fermat Potential of Embedded Spherical Lenses and the ISW Effect

The geometry of a CMB photon crossing an embedded lens of angular radius θ_M is sketched in Fig. 1. We assume a standard FLRW background universe with radius $R(t)$ in which last scattering occurs well before the CMB photons encounter the cluster or void of interest. In the homogeneous universe a CMB photon's frequency evolves with time according to $\nu_{3^\circ}(t) = \nu_{3^\circ} R(t_0)/R(t)$, reaching us at time t_0 with frequency ν_{3° . If this CMB photon is gravitationally lensed by an inhomogeneity at redshift z_d before reaching us, its frequency evolution is altered in its passage through the lens between points 1 and 2 (see Fig. 1). It

¹The notion of a Swiss cheese void should not be confused with a cosmic void. Cosmic voids are regions under-dense in gravitating matter and are often identified by looking for regions under-dense in galaxies.

enters the inhomogeneity at cosmic time t_1 with CMB frequency $\nu_{3^\circ}(t_1)$ and exits at time t_2 but with a frequency $\nu_{\text{sc}}(t_2)$, not equal to the CMB frequency $\nu_{3^\circ}(t_2)$, and then evolves again in the homogeneous FLRW background according to $\nu_{\text{sc}}(t) = \nu_{\text{sc}} R(t_0)/R(t)$, reaching us with frequency $\nu_{\text{sc}} \neq \nu_{3^\circ}$. Because all frequencies are similarly affected the temperature of the deflected photons will differ (after exiting) from those undeflected by

$$\frac{\Delta\mathcal{T}}{\mathcal{T}} = \frac{\nu_{\text{sc}} - \nu_{3^\circ}}{\nu_{3^\circ}}. \quad (1)$$

It is well known in conventional gravitational lensing theory that the arrival time at the observer of a photon emitted by a background source will be delayed if it is lensed by a foreground mass condensation, and that this time delay can be written as the sum of a geometrical and a potential part, $T = T_g + T_p$ (Cooke & Kantowski 1975). In conventional lensing theory time delay refers to the difference in arrival times of two separate lens images. In this work the time delay T refers to the delayed arrival time of a single lensed image compared to its would be arrival time in the absence of the lens. The difference in the T 's for two separate images gives their conventional arrival time difference. In all cases the time delays are of order r_s/c (the time it takes light to cross the Schwarzschild radius of the lens) and are small compared to the age of the universe. Within the conventional lensing theory the total time delay T we are introducing is proportional to the Fermat potential whose minimization, according to Fermat's least time principle (i.e., $\delta T/\delta\theta_I = 0$ where θ_I the image angle, see Fig. 1), gives the lens equation (Schneider 1985; Blandford & Narayan 1986). In Kantowski et al. (2013) we rigorously derived the lens equation for the embedded point mass lens and generalized that equation, at first order, to any spherically symmetric embedded lens

$$\theta_S = \theta_I - \frac{\theta_E^2}{\theta_I} [f(\theta_I/\theta_M, z_d) - f_{\text{RW}}(\theta_I/\theta_M)], \quad (2)$$

where θ_S and θ_I are the source and image angles, $\theta_E = \sqrt{2r_s D_{ds}/D_d D_s}$ is the standard Einstein ring angle (D_d , D_s and D_{ds} are respectively the angular diameter distances of the lens, the source, and the source with respect to the lens),

$$f_{\text{RW}}(x) \equiv 1 - \left[\sqrt{1-x^2}\right]^3, \quad 0 \leq x \leq 1, \quad (3)$$

is the projected mass fraction of the homogeneous sphere removed to form the Swiss cheese void ($x \equiv \theta_I/\theta_M$ is the normalized image angle), and $f(x, z_d) \equiv M(x\theta_M, z_d)/M(\theta_M)$ is the fraction of the lens' mass projected within the impact disk defined by θ_I at the lens redshift z_d (schematically shown in Fig. 1). For an inhomogeneity evolving at a rate different from the background FLRW universe, $f(x, z_d)$ depends on the cosmic time or equivalently the lens redshift z_d . We have rigorously derived the time-delay function, i.e., the Fermat potential

for the embedded point mass lens (see Eq. (7) in Kantowski et al. 2013). We now generalize that first order result and give the Fermat potential for any spherically symmetric embedded lens as

$$cT(\theta_S, \theta_I) = (1 + z_d) \frac{D_d D_s}{D_{ds}} \left[\frac{(\theta_S - \theta_I)^2}{2} + \theta_E^2 \int_x^1 \frac{f(x', z_d) - f_{\text{RW}}(x')}{x'} dx' \right]. \quad (4)$$

It is straightforward to check that variation of Eq. (4) with respect to the image angle θ_I gives the lens Equation (2). Equation (4) is essentially the same as the Fermat potential for a spherical lens under the thin lens approximation in the standard linearized lens theory (Schneider et al. 1992) except for the f_{RW} term which accounts for the (lowest order) effects of embedding (Kantowski et al. 2013). The term “Fermat potential” can refer to the two terms within the square brackets with or without the angular distances factor and/or the $1 + z_d$ factor. All factors are required for the use we make of it in this paper. The geometrical and potential parts of the time delay, i.e., T_g and T_p , are respectively the first and the second terms in Eq. (4). The key theoretical result in this paper is the relation of the *secondary* CMB temperature anisotropy (Sachs & Wolfe 1967; Rees & Sciama 1968) to a derivative of the potential part of the embedded lensing time delay,

$$\frac{\Delta \mathcal{T}}{\mathcal{T}} = H_d \frac{\partial T_p}{\partial z_d}, \quad (5)$$

where H_d is the Hubble parameter at the deflector’s redshift z_d , and from Eq. (4)

$$cT_p(\theta_I, z_d) = 2(1 + z_d)r_s \int_x^1 \frac{f(x', z_d) - f_{\text{RW}}(x')}{x'} dx'. \quad (6)$$

T_p in Eq. (5) can be replaced by the full time delay T (hence the Fermat potential) because the geometrical part T_g does not affect the CMB temperature, i.e., $\partial T_g / \partial z_d = 0$ (the source angle θ_S as well as the image angle θ_I are held fixed during the differentiation). We first investigate consequences of Eq. (5) and postpone its subtle derivation to Appendix A. A check of Eq. (5) for an embedded static lens appears in Appendix B.

Once $T_p(\theta_I, z_d)$ is known for a given lens, e.g., via integrating Eq. (6), temperature fluctuations $\Delta \mathcal{T}$ in the CMB caused by that lens can easily be found by taking the single derivative in Eq. (5). For an arbitrary lens we can understand the source of $\Delta \mathcal{T}$ by differentiating Eq. (6) without performing the integration. Because z_d appears in two places in Eq. (6), two terms contribute to the derivative, i.e., $\Delta \mathcal{T} = \Delta \mathcal{T}_{\text{T}} + \Delta \mathcal{T}_{\text{E}}$, where one term is proportional to the potential part of the time delay and is called the time-delay part

$$\frac{\Delta \mathcal{T}_{\text{T}}}{\mathcal{T}} = \frac{H_d T_p}{1 + z_d}, \quad (7)$$

and a second term called the evolutionary part

$$\frac{\Delta\mathcal{T}_E}{\mathcal{T}} = (1 + z_d) \frac{2r_s H_d}{c} \int_x^1 \frac{dx'}{x'} \frac{\partial f(x', z_d)}{\partial z_d}. \quad (8)$$

Time delays, T_p values in Eq. (7), produced by individual galaxies are too small to produce detectable effects on the CMB but time delays produced by large superclusters and huge voids are, see Fig. 2 and Table 1. The evolutionary part is only present when the perturbation evolves at a different rate than the background cosmology. We can relate these two parts to terms that appear when making a perturbative calculation of the ISW effect. If χ is the comoving radial coordinate measured from the center of the embedded lens, if $\tilde{\chi} \equiv \chi/\chi_b$ is the normalized comoving distance, and if $\rho(\tilde{\chi}, z_d)$ and $\bar{\rho}(z_d)$ are the matter densities of the embedded spherical lens and the homogeneous FLRW background universe, then the comoving density contrast of the lens is $\delta(\tilde{\chi}, z_d) \equiv (\rho - \bar{\rho})/\bar{\rho}$. Using Eq. (6) and the relation between projected and volume mass densities, the projected mass fraction can be written as

$$f(x, z_d) - f_{\text{RW}}(x) = 3 \int_0^x dy y \int_0^{\sqrt{1-y^2}} d\zeta \delta(\sqrt{y^2 + \zeta^2}, z_d), \quad (9)$$

and the total temperature fluctuation can be written in terms of the lens density contrast δ as

$$\frac{\Delta\mathcal{T}}{\mathcal{T}} = \frac{6r_s}{c/H_d} \int_x^1 \frac{dx'}{x'} \int_0^{x'} dy y \int_0^{\sqrt{1-y^2}} d\zeta \delta(\sqrt{y^2 + \zeta^2}, R_d) \left[1 - \frac{R_d}{\delta} \frac{\partial \delta}{\partial R_d} \right]. \quad (10)$$

The first and second terms within the square brackets correspond to the time-delay and evolutionary contribution, $\Delta\mathcal{T}_T$ and $\Delta\mathcal{T}_E$, respectively. In Eq. (10), $R_d \equiv R(t_0)/(1 + z_d)$ and is used as a ‘time’ variable rather than t_d . There is no time delay or temperature fluctuation at the boundary of the Swiss cheese void where $x = 1$ (i.e., $\theta_I = \theta_M$) for any embedded lens. For linearly evolving structures in an Einstein-de Sitter (EdS) universe, $\delta \propto R_d$ and the two terms in Eq. (10) exactly cancel resulting in $\Delta\mathcal{T} = 0$, consistent with the classical results of Sachs & Wolfe (1967). For linearly evolving structures in the standard Λ CDM universe, $|\delta|$ grows slower than R_d , and the evolutionary contribution only partially cancels the time-delay contribution resulting in a non-zero ISW effect (see Fig. 3 for an example). For highly non-linear structures (Bertschinger 1985a,b; Sheth & van de Weygaert 2004), $|\delta|$ might cease to grow or even start to decrease (e.g., a deep cosmic void with density contrast δ already approaching the lower bound -1), the evolutionary contribution can be of the same sign as the time-delay contribution. For such cases the time-delay contribution $\Delta\mathcal{T}_T$ can be used as a conservative estimate of the magnitude of the ISW signal (see the examples in the next Section). For embedded point mass lenses or lenses that expand with the background $f(x, z_d) = f(x)$ does not explicitly depend on z_d and the temperature fluctuation is simply

proportional to the time delay, see Eq. (7). The time-delay contribution to the temperature fluctuation is of the order $H_d T_p \sim H_d(2r_s/c) \sim 2\beta_d r_s/r_d$ where $c\beta_d \equiv H_d r_d$ is the expansion rate of the Swiss cheese void’s boundary relative to static observers and r_d is the physical radius of the void at redshift z_d (Kantowski et al. 2013). This is in line with estimates originally made in Rees & Sciama (1968) although the details differ. From Eq. (8) the evolutionary contribution is expected to be the same order of magnitude as long as only moderate expansion/contraction occurs.

3. Examples

To illustrate the simplicity of the embedded theory’s use, as well as to give an order of magnitude estimate of the effect on the CMB’s temperature fluctuations, we first construct simple embedded lens models for galaxy clusters and cosmic voids and then compute the late-time ISW effect by applying Eq. (5) to these models. We consider three centrally over-dense lenses (galaxy clusters) and three centrally under-dense lenses (cosmic voids). We assume the central mass densities of the embedded cluster lenses are homogeneous and expanding with the background, i.e., have constant angular radii $\bar{\theta}_M < \theta_M$ (see the central shaded region of Fig. 1). The projected mass fraction for this lens is $f_{\text{cluster}}(x) = f_{\text{RW}}(x/\bar{x})$ for $x \leq \bar{x}$ and equals 1 for $\bar{x} < x \leq 1$, where $\bar{x} \equiv \bar{\theta}_M/\theta_M$. From Eqs. (6) and (7) we obtain the temperature anisotropy for this simple cluster lens model

$$\frac{\Delta\mathcal{T}}{\mathcal{T}} = \frac{H_d}{1+z_d} \times \begin{cases} T_p^{\text{PM}}(x) - T_p^{\text{PM}}(x/\bar{x}), & \text{if } x \leq \bar{x}, \\ T_p^{\text{PM}}(x), & \text{if } \bar{x} < x \leq 1, \end{cases} \quad (11)$$

where $T_p^{\text{PM}}(x)$ is the Point Mass time delay given in Eq. (7) of Kantowski et al. (2013)

$$T_p^{\text{PM}}(x) = (1+z_d)\frac{2r_s}{c} \left(\log \left[\frac{1 + \sqrt{1-x^2}}{x} \right] - \frac{4-x^2}{3} \sqrt{1-x^2} \right). \quad (12)$$

In the left panel of Fig. 2 we give $\Delta\mathcal{T}$ for $\bar{x} = 0.5, 0.2$, and 0.1 , corresponding to respective density contrasts $\rho/\bar{\rho}$ of 8, 125, and 1000.

For voids the lensing picture is similar to Fig. 1 except the central region is an under-density and the deflection angle α is outward, i.e, a void is de-focusing rather than focusing. To be an exact solution of GR, Swiss cheese embedding requires the under-dense void interior to be surrounded by an over-dense bounding ridge. For simplicity we model a cosmic void as a uniform under-dense spherical region of density $\rho/\bar{\rho} = 1 + \delta = 0.1, 0.5$, or 0.9 (i.e., having density contrasts $\delta = -0.9, -0.5$ or -0.1 , see the right panel of Fig. 2) bounded by an over-dense thin shell which contains the mass removed from the homogeneous sphere (i.e.,

$f_{\text{shell}} = -\delta [1 - (1 - x^2)^{1/2}]$). If the voids are co-expanding δ remains constant; however, if they evolve δ changes with the deflector’s redshift z_d . For this void model

$$\frac{\Delta\mathcal{T}_T}{\mathcal{T}} = \delta \frac{2r_s}{3c/H_d} (1 - x^2)^{3/2}, \quad (13)$$

and

$$\frac{\Delta\mathcal{T}_E}{\mathcal{T}} = (1 + z_d) \frac{d \log \delta}{d z_d} \times \frac{\Delta\mathcal{T}_T}{\mathcal{T}}. \quad (14)$$

For simplicity we consider only two possibilities: the co-expanding case where $\delta'(z_d) \equiv d\delta/dz_d \equiv 0$ and only $\Delta\mathcal{T}_T$ contributes, and a linear evolving case where $\delta(z_d)$ is known from standard perturbation theory. Despite the extreme simplicity of this result, the model is useful for studying lensing by voids (Chen et al. 2015). Extension to other cluster or void models is straightforward. For example if the compensating ring of mass at the boundary of the Swiss cheese void in this simple model is moved inward it can produce a hot ring surrounding the void’s central cold spot.

In the left panel of Fig. 2 we plot the radial profile of the ISW effect across a super cluster at redshift $z_d = 0.5$ with an angular radius $\theta_M^{\text{cluster}} \simeq 1.2^\circ$. The cluster lens mass is $\sim 10^{16} M_\odot$. We test for three background cosmologies: an EdS universe ($\Omega_m = 1.0, \Omega_\Lambda = 0$), a concordance Λ CDM universe ($\Omega_m = 0.3, \Omega_\Lambda = 0.7$), and a baryonic-matter only universe ($\Omega_m = 0.05, \Omega_\Lambda = 0$), i.e., the left, middle, and right curves, respectively. From the left panel of Fig. 2 we see that for a cluster lens of fixed mass, the amplitude of the perturbation increases with central concentration (approaching the limiting case of an embedded point mass lens; $f_{\text{point}} = 1$). The CMB temperature increases by $\gtrsim 2 \mu\text{K}$ for a co-expanding cluster of $\sim 10^{16} M_\odot$ with density contrast $\delta \gtrsim 100$. The ISW signal predicted by the simple cluster model scales with the cluster mass, see Eqs. (11) and (12). Outside of the over-dense region, i.e., the vacuum, the cluster behaves exactly the same as a (static) point mass lens; inside the over-dense region, the lens might be still evolving. Consequently, prediction based on the simple model might be biased (e.g., increases more slowly near the cluster center than predicted in Fig. 2). However, since the over-dense region takes only a small fraction of the lens volume, our model should give reasonable estimate for the averaged signal for rich galaxy clusters ($\langle \Delta T \rangle$ about $\sim 0.3 \mu\text{K}$ for a $10^{16} M_\odot$ cluster assuming $\delta \gtrsim 100$). More physical embedded cluster model (e.g., non-uniform density profile with different evolution scenarios) will be pursued in future works (e.g., Kantowski et al. 2014). We also see that various background cosmologies influence $\Delta\mathcal{T}_T$ through the Hubble parameter H_d ; however, the differences are not very significant.

The right panel of Fig. 2 and Table 1 show predictions for the two simple void lens models (co-expanding and linearly evolving) at redshift $z_d = 0.5$. The concordance void lens has angular radius $\theta_M^{\text{void}} \simeq 2^\circ$ with physical radius $r_d \approx 40 \text{ Mpc}$ and mass $\sim 4.8 \times 10^{16} M_\odot$. The

Table 1. Amplitudes of ISW cold spots produced by compensated voids in the concordance Λ CDM cosmology. CMB temperature reductions in μK are given for Swiss cheese voids of radii $r_d = 5, 20, 50,$ and 100 Mpc at redshifts $z = 0.5$ and 1.0 with density contrasts $\delta = (\rho - \bar{\rho})/\bar{\rho} = -0.1, -0.5,$ and -0.9 . The comoving cosmic mass M_d contained in the void radius r_d is also given as well as its angular size θ_M .

$\Delta\mathcal{T}$ (μK)	$r_d = 5$ Mpc	20 Mpc	50 Mpc	100 Mpc
$z_d = 0.5$	$M_d = 7.2 \times 10^{13} M_\odot$ $\theta_M = 0.23^\circ$	$4.6 \times 10^{15} M_\odot$ 0.91°	$7.2 \times 10^{16} M_\odot$ 2.3°	$5.8 \times 10^{17} M_\odot$ 4.6°
$\delta = -0.1$	$(-0.0001, -0.00038)^a$	$(-0.006, -0.025)$	$(-0.096, -0.38)$	$(-0.77, -3.06)$
$\delta = -0.5$	$(-0.0005, -0.0019)$	$(-0.031, -0.12)$	$(-0.479, -1.91)$	$(-3.83, -15.29)$
$\delta = -0.9$	$(-0.0009, -0.0034)$	$(-0.055, -0.22)$	$(-0.861, -3.44)$	$(-6.89, -27.52)$
$z_d = 1.0$	$M_d = 1.7 \times 10^{14} M_\odot$ $\theta_M = 0.17^\circ$	$1.1 \times 10^{16} M_\odot$ 0.69°	$1.7 \times 10^{17} M_\odot$ 1.7°	$1.4 \times 10^{18} M_\odot$ 3.5°
$\delta = -0.1$	$(-0.00016, -0.0012)$	$(-0.01, -0.078)$	$(-0.16, -1.22)$	$(-1.27, -9.77)$
$\delta = -0.5$	$(-0.0008, -0.0061)$	$(-0.05, -0.39)$	$(-0.79, -6.10)$	$(-6.35, -48.85)$
$\delta = -0.9$	$(-0.0014, -0.011)$	$(-0.09, -0.70)$	$(-1.43, -10.97)$	$(-11.43, -87.93)$

^aThe number pairs are for linearly evolving voids (left) and co-expanding voids (right) respectively. The value for the linearly evolving case is about a factor of 0.25 and 0.13 of the value for the co-expanding case for $z_d = 0.5$ and 1.0 , respectively (see Fig. 3).

dashed and solid curves show the results for co-expanding and linearly evolving void models, respectively. The signal scales linearly with the lens mass r_s (equivalently as the cube of the void size θ_M) and emptier voids result in colder CMB spots, i.e., they scale with δ . From Fig. 2 the CMB temperature is seen to decrease by $\gtrsim 1.5 \mu\text{K}$ for a co-expanding void of radius $\theta_M \gtrsim 2^\circ$ if $\delta \lesssim -0.5$. For a void evolving relative to the background cosmology there is an additional contribution to the temperature profile, the evolutionary part. If the void evolves according to standard linear perturbation theory, then the evolutionary contribution $\Delta T_{\mathcal{E}}$ of Eq. (14) significantly cancels the time-delay contribution $\Delta \mathcal{T}_T$ of Eq. (13) (see Fig. 3). The cancellation is complete for an EdS cosmology as expected, and the total $\Delta \mathcal{T}$ is reduced by 75% and 20% of the time-delay contribution respectively for ΛCDM and baryonic-matter only universes. Cosmic voids discovered from galaxy surveys have radii from $\sim 5 \text{ Mpc}$ to $\sim 100 \text{ Mpc}$ with majority of them having radii of the order of $\sim 10 \text{ Mpc}$ (Sutter et al. 2012). In Table 1 we estimate the magnitude of the ISW cold spot caused by cosmic voids having different void sizes and density contrasts. We present results for both the linearly evolving and co-expanding scenarios and test for two redshift $z_d = 0.5$ and 1. For small density contrast (e.g., $\delta = -0.1$) linear perturbation theory should give a better estimate of the ISW signal, whereas for large density contrast (e.g., $\delta = -0.9$), the co-expanding model should give a better estimate. The two numbers can be used as approximate lower and upper bounds for the ISW signal caused by cosmic voids.

Figure 3 shows the redshift dependence of the amplitude of the ISW effect for the two simple void lens models presented in this paper. We plot the growth curves of the ISW effect with redshift for the time-delay contribution $\Delta \mathcal{T}_T$, evolutionary contribution $\Delta \mathcal{T}_{\mathcal{E}}$ assuming linear perturbation theory, and the sum of the two contributions (the blue, red, and black curves respectively). To compute the ISW temperature profiles for a void at an arbitrary redshift z , you simply scale the curves in the right panel of Fig. 2 ($z_d = 0.5$) using the corresponding curves in Fig. 3, i.e., apply a multiplicative factor $\text{ISW}_T(z)/\text{ISW}_T(0.5)$ and $\text{ISW}(z)/\text{ISW}(0.5)$ for the co-expanding and linear evolving model respectively. The reader can observe from the left panel, as stated earlier, that linearly evolving perturbations in an EdS universe do not directly alter the CMB’s temperature, i.e., the net growth factor vanishes $\text{ISW}(z) = 0$ for all z . What is clear for the other two cosmologies is that for the highest redshifts ($z > 20$) the earlier in cosmic time they are encountered the less they perturb the CMB. However, somewhat closer voids ($20 > z > 0$) in an open baryonic matter universe (see the black curve in the third panel) will produce larger effects on CMB temperatures with increasing redshifts, whereas, voids in a concordance universe (see the black curve in the middle panel) have a rapidly diminishing effect (with increasing redshift) on the CMB for all $z > 0$. Seeing a decrease in ISW temperatures with redshift is clearly expected if we do live in a concordance universe.

Figure 4 shows an example of ISW-induced CMB temperature fluctuations (with and without linear evolution) using the recent void catalogue from SDSS DR7 (Sutter et al. 2012; Abazajian et al. 2009) and the void models described above. For simplicity we have assumed the same density contrast $\delta = -0.5$ for all voids (density profiles for individual cosmic voids are not available, only mean profiles have been estimated by stacking/averaging a large number of cosmic voids). The majority of the voids have radii of the order of ~ 10 Mpc, and their evolution can be non-linear. Consequently, the time-delay contribution $\Delta\mathcal{T}_T$ (the left panel) might give better estimates of the ISW signals. For those really large voids (with radius ~ 80 Mpc), if they are shallow as predicted by standard theory, then linear perturbation theory should give better estimates of the signal (the right panel). Because most of the voids are at low redshifts ($z \lesssim 0.5$), the ISW signal of the linear evolution scenario is about one third to one fourth of the time-delay contribution because of the cancellation of $\Delta\mathcal{T}_T$ by $\Delta\mathcal{T}_E$ (see Fig. 3). Consequently, the right panel looks very similar to the left panel except for the color-bar. Assuming a different void density contrast will also result in a similar figure except for a pure rescaling of the color-bar. For example, if we chose $\delta = -0.1$ instead of $\delta = -0.5$, then the signal will be reduced to one fifth of its current values for both scenarios.

4. Discussions and Conclusions

Granett et al. (2008a) claimed a detection of the ISW effect at $-11.3 \pm 3.1 \mu\text{K}$ by stacking 50 of the largest voids (effective radius $\gtrsim 100$ Mpc) from their catalog using the WMAP 5-year data. Similar analyses have also been conducted for the same and other void catalogs (Sutter et al. 2012; Pan et al. 2012; Nadathur & Hotchkiss 2014) by several other groups using WMAP or *Planck* data (e.g., Ilić et al. 2013; Cai et al. 2014; Planck Collaboration 2014b; Hotchkiss et al. 2015). Analyses of the more recent catalogs have typically given signals of more moderate amplitude and lower significance (from negligible to $\sim 2.5 \sigma$; Ilić et al. 2013; Planck et al. 2014b). For example, Ilić et al. (2013) confirmed the Granett et al. (2008a) results (at slightly lower significance) using WMAP 7-year data. They detected no signals using the Pan et al. (2012) catalog and a signal up to $\sim 2.4 \sigma$ using the Sutter et al. (2012) catalog (after rescaling of the voids to the same size on the stacked images). Recently the amplitude of the Granett et al. (2008a) detection has been re-confirmed by *Planck* by applying the aperture photometry method to *Planck* CMB temperature maps and the same void catalog (Planck Collaboration 2014b). Several groups found that the observed CMB fluctuations from stacking and averaging cosmic voids are significantly larger than expected from the linear ISW effect. For example, Nadathur et al. (2012) found a theoretical value from a linear perturbation analysis in ΛCDM cosmology $\gtrsim -2 \mu\text{K}$, inconsistent with the observed value from Granett et al. (2008a) at $> 3 \sigma$. Numerical simulations have also predicted

smaller effects (Maturi et al. 2007; Cai et al. 2010, 2014; Flender et al. 2013; Watson et al. 2014; Hotchkiss et al. 2015). For example, Cai et al. (2014) found a cold ISW imprint of amplitude between 2.6 and 2.9 μK and significance of $\sim 2\sigma$ using voids selected in the SDSS DR7 spectroscopic redshift galaxy catalog calibrated by N-body simulations. A Λ CDM signal consistent with zero was predicted by Hotchkiss et al. (2015) using the Jubilee N-body simulation and confirmed using a catalogue of voids and superclusters extracted from SDSS, thus challenging all positive ISW interpretations.

We tentatively compare predictions based on our simple embedded void model with recent observations based on void-stacking (Granett et al. 2008a; Planck Collaboration 2014b). The time delay of a deep cosmic void ($\delta = -0.9$) of angular radius $\sim 4^\circ$ at $z_d = 0.5$ (about the mean radius and redshift for the 50 voids in Granett et al. 2008a) results in $\Delta\mathcal{T} \approx -18.8 \mu K$ toward the void center and an averaged cold spot of about $-7.5 \mu K$ after convolving with a compensated top-hat filter of aperture radius $\theta_F = 4^\circ$. These temperature reductions are of the same order as observed from stacking and averaging large cosmic voids in the Granett et al. (2008a) catalog (Granett et al. 2008a; Planck Collaboration et al. 2014b). However, to produce an effect of this order of magnitude requires those large voids to be very deep, $\delta \sim -0.9$ and/or possibly evolve in an unknown non-linear way. Cosmic voids in galaxy surveys were selected as regions with low galaxy number densities; however, luminous matter as a tracer of dark matter might be biased. The dark matter density contrast within a cosmic void might be shallower than the $\delta \sim -0.9$ estimate based on galaxy number counts (Sutter et al. 2012, 2014). If the void is much shallower, as predicted by standard theory, then the ISW effect will not be able to produce signals of the order of the recent detections. For example, if we assume $\delta = -0.5$ (still a large density contrast), then estimates based on time delays alone are not sufficient because the void is probably still evolving and the evolutionary contribution needs to be included (see Fig. 3). For linear evolution, our model predicts a signal of the order of $\sim 2 \mu K$, similar to results of other predictions (Nadathur et al. 2012; Flender et al. 2013; Ilić et al. 2013; Cai et al. 2010, 2014). Calibrating the galaxy bias for void catalogs is an active field of research (Rasset et al. 2007; Szapudi et al. 2014a,b; Hamaus et al. 2014; Leclercq et al. 2014). A linear galaxy bias $b_g = 1.41 \pm 0.07$ was recently used by Szapudi et al. (2014a,b) to model the CMB Cold Spot using the ISW effect caused by a super giant void of radius $192 \pm 15 h^{-1}$ Mpc and density contrast $\delta = -0.13 \pm 0.03$ (see also Finelli et al. 2014). Similar estimate on b_g was obtained earlier by Rassat et al. (2007) for galaxies selected from the Two Micron All Sky Survey (Jarrett et al. 2000). The galaxy void profiles of Sutter et al. (2012) suggest very low density near the void center, $\delta \lesssim -0.8$ for voids of radii range from a few up to ~ 100 Mpc. For simplicity, we have assumed a uniform dark matter density contrast $\delta = -0.5$ for all voids (large and small) when simulating the CMB sky map modulated by ISW effect caused by cosmic voids (see Fig 4). This is

equivalent to assuming a linear galaxy bias $b_g \approx 1.8$ for all voids (see Fig. 9 of Sutter et al. 2012). For simplicity, we have also assumed all voids to be compensated (with zero net mass with respect to the homogeneous background). Numerical simulations show that small voids tend to be over-compensated, while large voids might be under-compensated (Sheth & van de Weygaert 2004; Ceccarelli et al. 2013; Hamaus et al. 2014; Cai et al. 2014). More accurate modeling using more physical density profiles and better estimates of galaxy bias (Sutter et al. 2014; Hamaus et al. 2014; Leclercq et al. 2014) is beyond the scope of the paper but is important to pursue in further work.

The new results of this paper are Eqs. (4)–(6), which result in Eqs. (7)–(10), i.e., simple analytical expressions for *secondary* temperature anisotropies in the CMB caused by encountering mass inhomogeneities, i.e., embedded gravitational lenses. The temperature fluctuations are obtained from a simple derivative of the Fermat potential. That derivative is the same as a derivative of the potential part of the time delay which is easy to compute for an arbitrary lens model via Eq. (6). This new method of obtaining CMB temperature changes represents a significant improvement over previous methods. We find that the CMB temperature change, i.e., $\Delta\mathcal{T}$ given in Eq. (5), can be understood as coming from two sources. The first source of change is the time delay and occurs because the increase in the Swiss cheese void’s radius depends on how long the lens mass delays the passing photon. The longer it is delayed the larger the cosmic expansion and the more the unlensed CMB photons are redshifted. This term is given in Eq. (7). Clusters tend to delay lensed photons making them bluer and voids shorten transit times making them redder. A second source of temperature change is the evolution of the distribution of the embedded mass inside the Swiss cheese void relative to the background cosmology, i.e., a f and δ dependence on cosmic time alters the frequency of the transiting photon. This temperature change can be positive or negative depending on lens details and is given in Eq. (8). We have confirmed Eqs. (7) and (8) by comparing results with prior analytic examples, e.g., the embedded expanding homogeneous dust sphere model (Dyer 1976), and the compensated void/lump model under the potential approximation (Martínez-González et al. 1990). We have used Eq. (8) in Fig. 3 to estimate the effect of linear perturbation growth of the voids temperature profiles of Fig. 2. Our theory is valid for arbitrarily large density contrast and is therefore very useful for studying CMB lensing in nonlinear regimes, e.g., lensing by cosmic voids where the density contrast can be large (Sutter et al. 2012, 2014) and by galaxy clusters where $\delta \gg 1$. For individual nonlinear cosmic structures, the temperature fluctuation can be easily computed provided that the expanding/collapsing histories of the structures are known from astrophysical theories or simulations (Press & Schechter 1974; Bertschinger 1985a,b; Sheth & van de Weygaert 2004). This is in contrast to the standard linear ISW analysis where the Poisson equation for the perturbation potential (or the density contrast) is solved

in Fourier space with some assumed initial power spectrum. Such an approach is not convenient for modeling temperature fluctuations caused by individual structures with a fixed scale, whereas our embedded theory is. We found that to produce secondary anisotropies of the order of some recent measurements of the ISW effect made using the void-stacking method requires large cosmic voids to be more numerous, deeper, and evolving differently than predicted by linear perturbation theory.

A. Proof of Equation (5)

Suppose two identical CMB photons with frequencies $\nu_{3^\circ}(t_1)$ reach the embedded lens at comoving point 1 in Fig. 1 at cosmic time t_1 . One photon is gravitationally deflected by the embedded lens and exits at comoving point 2 at time t_2 on a path differing in direction by an angle α . The second photon is reflected by an angle α at point B as it travels from point 1 to point 2 on two straight line segments, just as if the embedded lens didn't exist. The lensed photon exits comoving point 2 at cosmic time t_2 which is later than the reflected photon by an amount of time $T_p(t_2)$ which is by definition the potential part of the time delay (Chen et al. 2010). After leaving point 2, both photons travel the same comoving path but with the reflected photon leading the delayed gravitationally lensed photon in time by $T_p(t) = T_p(t_0)R(t)/R(t_0)$.² Because both photons had the same frequency ν_1 and period δt_1 at t_1 the ratio of the lensed photon's frequency at t_2 to the reflected photon's frequency at $t_2 - T_p(t_2)$ is given by the inverse ratio of their periods, $\delta(t_2 - T_p(t_2))/\delta t_2$. Because all photons redden equally after t_2 the ratio of the frequencies of lensed to unlensed CMB photons at equal t is constant and is given by

$$\begin{aligned} \frac{\nu_{\text{sc}}(t)}{\nu_{3^\circ}(t)} &= \frac{R(t)}{R(t - T_p(t))} \times \frac{\nu_{\text{sc}}(t)}{\nu_{3^\circ}(t - T_p(t))} \\ &= \frac{R(t)}{R(t - T_p(t))} \times \frac{\delta(t - T_p(t))}{\delta t}. \end{aligned} \tag{A1}$$

This analytic expression can be evaluated at the cosmic time t_d equivalent to the redshift z_d of the deflector, giving

$$\frac{\nu_{\text{sc}}}{\nu_{3^\circ}} = 1 + H_d \frac{\partial [(1 + z_d)T_p(z_d)]}{\partial z_d}. \tag{A2}$$

The quantity $T_p \equiv (1 + z_d)T_p(z_d)$ is the potential part of the time delay as seen at the observer given in Eq. (6), written as a function of the deflector's redshift. When Eq. (A2) is used in Eq. (1), Eq. (5) results. Equation (A1) can be interpreted as a product of a time-delay

²This is an approximation that requires $H_d T_p \ll 1$.

effect and a redshift effect associated with the density evolution. The evolutionary effect is produced by a time dependence in the projected mass fraction, see Eq. (8), or equivalently in the relative mass density, see Eq. (10), and is hence associated with a time dependence of the Newtonian potential of the relative perturbation.

B. The ISW/RS Effect for an Embedded Point Mass Lens

Because Eq. (5) is new and its derivation in Appendix A is subtle we wish to confirm its validity by comparing its prediction for the late-time ISW/RS effect caused by an embedded point mass with the prediction made by the conventional approach. The conventional approach dates back to Rees & Sciama (1968) and requires a detailed calculation of the photon’s deflected orbit. Equation (2) of Dyer (1976) gives the needed ratio of observed frequencies of a lensed CMB photon ν_{sc} to an identical unlensed CMB photon ν_{3°

$$\frac{\nu_{\text{sc}}}{\nu_{3^\circ}} = \frac{R(t_2) \nu_{\text{sc}}(t_2)}{R(t_1) \nu_{\text{sc}}(t_1)}, \quad (\text{B1})$$

where all frequencies are measured by observers comoving with the background FLRW cosmology. This equality is a result of both lensed and unlensed photons being identically redshifted after lensing (after the lensed photon exits at cosmic time t_2 with frequency $\nu_{\text{sc}}(t_2)$, see point 2 of Fig. 1) and both photons having the same frequencies prior to lensing which begins at t_1 with frequency $\nu_{3^\circ}(t_1) = \nu_{\text{sc}}(t_1)$.

Using Eqs. (9) and (10) of Kantowski et al. (2010) and details of the photon’s orbit that follow, Eq. (B1) can be evaluated to give the ISW/RS effect for a flat background universe, but only after a significant amount of algebra. The result is

$$\begin{aligned} \frac{\mathcal{T} + \Delta\mathcal{T}}{\mathcal{T}} &= \frac{R(t_2) \nu_{\text{sc}}(t_2)}{R(t_1) \nu_{\text{sc}}(t_1)} = \\ &= 1 - \left[\frac{\beta_1 r_s}{6 r_0} \left(15 \cos \tilde{\phi}_1 + \cos 3\tilde{\phi}_1 + 12 \log \tan \frac{\tilde{\phi}_1}{2} \right) \sin \tilde{\phi}_1 - \frac{2 r_s}{3 r_0} \Lambda r_0^2 \cos^3 \tilde{\phi}_1 \cot \tilde{\phi}_1 \right. \\ &\quad \left. - \frac{3 r_s^2}{4 r_0^2} \sin^2 \tilde{\phi}_1 \cos \tilde{\phi}_1 \left(7 \cos \tilde{\phi}_1 + \cos 3\tilde{\phi}_1 + 4 \log \tan \frac{\tilde{\phi}_1}{2} \right) \right], \quad (\text{B2}) \end{aligned}$$

where the photon’s orbit has been used to give its exit time t_2 and exit frequency $\nu_{\text{sc}}(t_2)$ as a function of its entry angle $\tilde{\phi}_1$ and its minimum radial Kottler coordinate r_0 . The reader is directed to Fig. 1 of Kantowski et al. (2010) for the definition of the entrance angle $\tilde{\phi}_1$ and minimal radial coordinate r_0 , and to Eq. (8) for a definition of the expansion rate β_1 of the lens void’s boundary at entry point 1. The reader is now in a position to appreciate the

simplicity of using Eq. (5) rather than Eq. (B2) to evaluate the ISW effect. The potential part of the time delay for the embedded point mass is given in Eq. (12) from which a simple derivative with respect to z_d in Eq. (5) gives Eq. (7) which is proportional to the time delay $T_p^{\text{PM}}(\theta_I/\theta_M)$ itself, i.e., for this lens

$$\frac{\Delta\mathcal{T}}{\mathcal{T}} = \frac{\Delta\mathcal{T}_T}{\mathcal{T}} = \frac{H_d T_p^{\text{PM}}(\theta_I/\theta_M)}{1 + z_d}. \quad (\text{B3})$$

To compare Eq. (B2) with Eq. (B3) the Kottler impact variables β_1 , $\tilde{\phi}_1$, and r_0 in Eq. (B2) must be converted to image positions θ_I , expansion velocities β_d , lens sizes r_d , and maximum image positions θ_M all evaluated at fixed cosmic time t_d defined by the deflector's redshift $1 + z_d = R(t_0)/R(t_d)$. The needed change of variables given in the next three equations can be found in Eq. (3) of Kantowski et al. (2013), Eq. (A1) of Kantowski et al. (2013), and Eqs. (2) and (15) of Chen et al. (2011)

$$\begin{aligned} \tilde{\phi}_1 &= \sin^{-1} \frac{\theta_I}{\theta_M} + \delta \beta_d \frac{\theta_I}{\theta_M} + \mathcal{O}(\delta^2), \\ r_0 &= r_d \sin \tilde{\phi}_1 (1 - \delta \beta_d \cos \tilde{\phi}_1) + \mathcal{O}(\delta^2), \\ \beta_1 &= \beta_d + \delta \left(\frac{r_s}{2r_d} - \frac{\Lambda r_d^2}{3} \right) \cos \tilde{\phi}_1 + \mathcal{O}(\delta^3), \end{aligned} \quad (\text{B4})$$

and results in Eqs. (B2) and (B3) giving identical results for $\Delta\mathcal{T}/\mathcal{T}$ to order δ^1 .

The reader can easily see that because there is no time evolution of the projected mass fraction ($f(\theta_I/\theta_M) = 1$) or equivalently in the density contrast ($\delta = -1$) for an embedded point mass, only the time delay part, Eq. (7), contributes to the ISW effect.

REFERENCES

- Abazajian, K. N., Adelman-McCarthy, J. K., Agüeros, M. A, et al. 2009, *ApJS*, 182, 543
 Bennett, C. L., Halpern, M., Hinshaw, G., et al. 2003, *ApJS*, 148, 1
 Bertschinger, E. 1985a, *ApJS*, 58, 1
 Bertschinger, E. 1985b, *ApJS*, 58, 39
 Birkinshaw, M. 1999, *Phys. Rep.*, 310, 97
 Blandford, R., & Narayan, R. 1986, *ApJ*, 310, 568
 Boughn, S., & Crittenden, R. 2004, *Nature*, 427, 45

- Cai, Y-C., Cole, S., Jenkins, A., & Frenk, C. S. 2010, MNRAS, 407, 201
- Cai, Y-C., Neyrinck, M. C., Szapudi, I., et al. 2014, ApJ, 786, 110
- Ceccarelli, L., Paz, D., Lares, M., et al. 2013, MNRAS, 434, 1435
- Chen, B., Kantowski, R., & Dai, X. 2010, Phys. Rev. D, 82, 043005
- Chen, B., Kantowski, R., & Dai, X. 2011, Phys. Rev. D, 84, 083004
- Chen, B., Kantowski, R., & Dai, X. 2015, ApJ, in press (arXiv1310.7574)
- Cole, S., & Efstathiou, G. 1989, MNRAS, 239, 195
- Cooke, J. H., & Kantowski, R. 1975, ApJ, 195, L11
- Cooray, A. 2002a, Phys. Rev. D, 65, 083518
- Cooray, A. 2002b, Phys. Rev. D, 65, 103510
- Cooray, A., & Seto, N. 2005, J. Cosmology Astropart. Phys., 0512, 004
- de Lapparent, V., Geller, M. J., Huchra, J. P. 1986, ApJ, 302, 1
- Dyer, C. C. 1976, MNRAS, 175, 429
- Dupé, F.-X., Rassat, A., Starck, J.-L., Fadili, M. J. 2011, A&A, 534, 51
- Einstein, A., & Straus, E. G. 1945, Rev. Mod. Phys., 17, 120
- Eisenstein, D. J., Zehavi, I., Hogg, D. W., et al. 2005, ApJ, 633, 560
- Finelli, F., García-Bellido, J., Kovács, A., Paci, F., Szapudi, I. 2014, MNRAS, submitted, arXiv1405.1555
- Flender, S., Hotchkiss, S., & Nadathur, S. 2013, J. Cosmology Astropart. Phys., 02, 013
- Granett, B. R., Neyrinck, M. C., & Szapudi, I. 2008a, ApJ, 683, 99
- Granett, B. R., Neyrinck, M. C., & Szapudi, I. 2008b, arXiv.0805.2974
- Hamaus, N., Sutter, P. M., Wandelt, B. D. 2014, Phys. Rev. Lett., 112, 251302
- Hernández-Monteagudo, C. 2010, A&A, 520, 101
- Hernández-Monteagudo, C., & Smith R. E. 2013, MNRAS, 435, 1094

- Ho, S., Hirata, C., Padmanabhan, N., et al. 2008, *Phys. Rev. D*, 78, 043519
- Hotchkiss, S., Nadathur, S., Gottlöber, S., et al. 2015, *MNRAS*, 446, 1321
- Hu, W. 2000, *ApJ*, 529, 12
- Ilić, S., Langer, M., & Douspis, M. 2013, *A&A*, 556, 51
- Inoue, K. T., & Silk, J. 2006, *ApJ*, 648, 23
- Jarrett T. H., Chester T., Cutri R., et al. 2000, *AJ*, 119, 2498
- Kantowski, R., Chen, B., & Dai, X. 2010, *ApJ*, 718, 913
- Kantowski, R., Chen, B., & Dai, X. 2012, *Phys. Rev. D*, 86, 043009
- Kantowski, R., Chen, B., & Dai, X. 2013, *Phys. Rev. D*, 88, 083001
- Kantowski, R., Chen, B., & Dai, X. 2014, *Phys. Rev. D*, in press, arXiv1410.4608
- Kim, J., Rotti, A., & Komatsu, E. 2013, *J. Cosmology Astropart. Phys.*, 04, 021
- Kottler, F. 1918, *Ann. Phys., Lpz.*, 361, 401
- Leclercq, F., Jasche, J., Sutter, P. M., et al. 2014, arXiv1410.0355
- Martínez-González, E., Sanz, J. L., & Silk, J. 1990, *ApJ*, 355, L5
- Maturi, M., Dolag, K., Waelkens, A., et al. 2007, *A&A*, 476, 83
- Miralda-Escudé, J., Haehnelt, M., & Rees, M. J. 2000, *ApJ*, 530, 1
- Nadathur, S., Hotchkiss, S., & Sakar, S. 2012, *J. Cosmology Astropart. Phys.*, 06, 042
- Nadathur, S., Lavinto, M., Hotchkiss, S., & Räsänen, S. 2014, *Phys. Rev. D*, 90, 103510
- Nadathur, S., Hotchkiss, S. 2014, *MNRAS*, 440, 1248
- Nottale, L. 1984, *MNRAS*, 206, 713
- Pan, D. C., Vogele, M. S., Hoyle, F., et al. 2012, *MNRAS*, 421, 926
- Panek, M. 1992, *ApJ*, 388, 225
- Perlmutter, S., Aldering, G., Goldhaber, G., et al. 1999, *ApJ*, 517, 565
- Planck Collaboration, Ade, P. A. R., et al. 2014a, *A&A*, 571, 24

- Planck Collaboration, Ade, P. A. R., et al. 2014b, *A&A*, 571, 19
- Press, W. H., & Schechter, P. 1974, *ApJ*, 187, 425
- Rassat, A., Land, K., Lahav, O., Abdalla, F. B. 2007, *MNRAS*, 377, 1085
- Rees, M. J., & Sciama, D. W. 1968, *Nature*, 217, 511
- Riess, A. G., Filippenko, A. V., Challis, P., et al. 1998, *AJ*, 116, 1009
- Rudnick, L., Brown, S. & Williams, L. R. 2007, *ApJ*, 671, 40
- Sachs, R. K., & Wolfe, A. M. 1967, *ApJ*, 147, 73
- Sakai, N., & Inoue, K. T. 2008, *Phys. Rev. D*, 78, 063510
- Schneider, P. 1985, *A&A*, 143, 413
- Schneider, P., Ehlers, J., & Falco, E. E. 1992, *Gravitational Lenses* (1st ed.; Berlin: Springer-Verlag).
- Schücking, E. 1954, *Z. Phys.*, 137, 595
- Seljak, U. 1996a, *ApJ*, 463, 1
- Seljak, U. 1996b, *ApJ*, 460, 549
- Sheth, R. K., & van de Weygaert, R. 2004, *MNRAS*, 350, 517
- Smith, R. E., Hernández-Monteagudo, C., Seljak, U. 2009, *Phys. Rev. D*, 80, 063528
- Sunyaev, R. A., & Zeldovich, Y. B. 1980, *MNRAS*, 190, 413
- Sutter, P. M., Lavaux, G., Wandelt, B. D., & Weinberg, D. H. 2012, *ApJ*, 761, 44
- Sutter, P. M., Lavaux, G., Wandelt, B. D., & Weinberg, D. H., Warren, M. S. 2014, *MNRAS*, 438, 3177
- Szapudi, I., Kovács, A., Cranett, B. R., et al. 2014, *MNRAS*, submitted, arXiv1405.1566
- Szapudi, I., Kovács, A., Cranett, B. R., et al. 2014, arXiv1406.3622
- Tegmark, M., de Oliveira-Costa, A., & Hamilton, A. J. S. 2003, *Phys. Rev. D*, 68, 123523
- Valkenburg, W. 2009, *J. Cosmology Astropart. Phys.*, 06, 010
- Vielva, P., Martínez-González, E., Barreiro, R. B., et al. 2004, *ApJ*, 609, 22

Vishniac, E. T. 1987, *ApJ*, 322, 597

Watson, W. A., Diego, J. M., Gottlöber, S., et al. 2014, *MNRAS*, 438, 412

Zeldovich, Y. B., & Sunyaev, R. A. 1969, *Ap&SS*, 4, 301

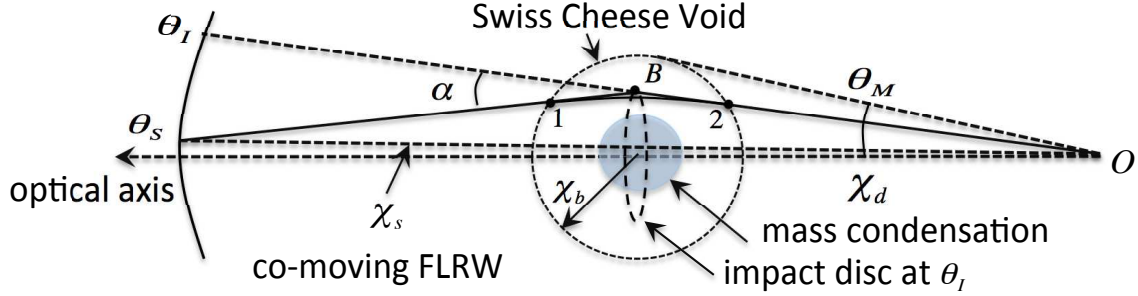


Fig. 1.— The comoving geometry of an embedded cluster lens. θ_S and θ_I are the source and image angles, respectively; χ_d and χ_s are respective comoving distances of the lens and the source. The (constant) angular size of the void is $\theta_M \equiv \chi_b/\chi_d$ where χ_b is the comoving radius of the void whose physical radius is $r_d = R(t_d)\chi_b$ at cosmic time t_d defined by the deflector’s redshift $1 + z_d = R_0/R(t_d)$. The shadowed area represents the extended spherically symmetric mass condensation of the cluster. The dashed circle shows the impact disc of angular radius θ_I used to compute the projected mass fraction f used in Eqs. (2)-(9). The equivalent figure for a void has a mass condensation surrounding a low density central region and an outward deflection angle α .

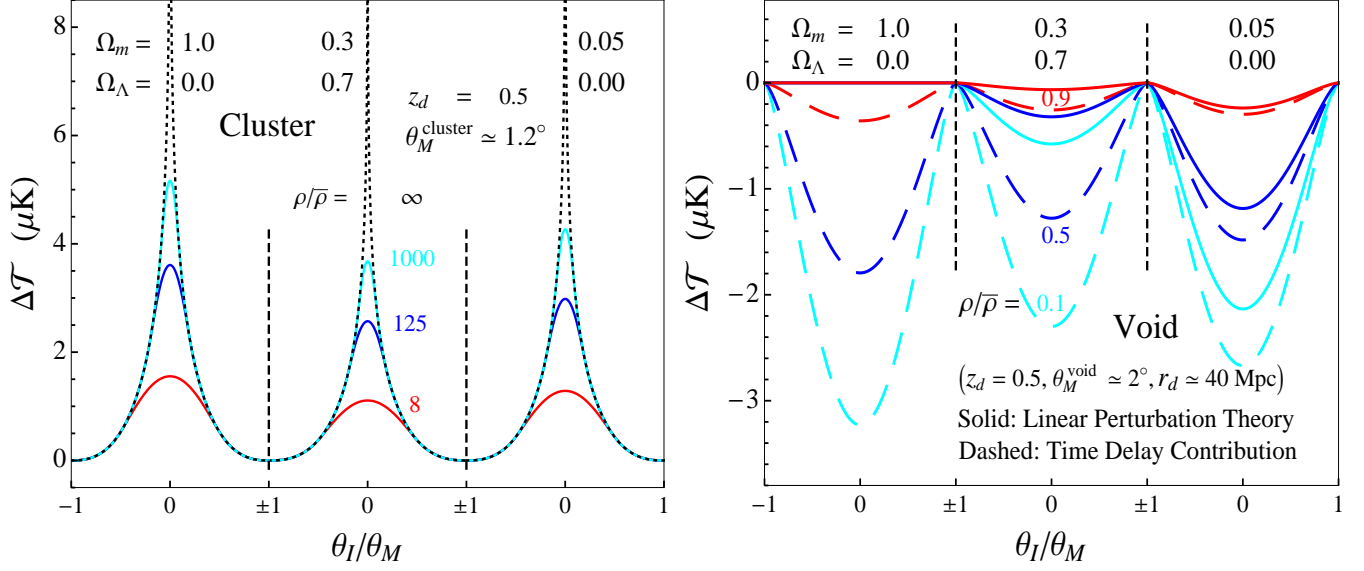


Fig. 2.— Secondary anisotropies in the CMB across an embedded super cluster lens of angular size $\theta_M \simeq 1.2^\circ$ and a void lens of size $\theta_M \simeq 2^\circ$ (respectively left and right panels) both at $z_d = 0.5$. Three background FLRW cosmologies are shown in each panel: the Einstein-de Sitter universe (left curves), the concordance ΛCDM universe (middle curves), and an open baryonic-matter only universe (right curves). The concordance cluster and void lens masses are about $10^{16} M_\odot$ and $4.8 \times 10^{16} M_\odot$, respectively. For the cluster lens $\Delta\mathcal{T}$ (in μK) is shown for four models: three uniformly distributed mass condensations with central over-densities $\rho/\bar{\rho} = 8, 125$, and 1000 , all co-expanding with the background cosmologies (the respective solid red, blue and cyan curves), and for a point mass condensation (the dotted curves). In the right panel cosmic voids are modeled as uniformly under-dense spherical regions of densities $0.1\bar{\rho}, 0.5\bar{\rho}$, and $0.9\bar{\rho}$ bounded by thin walls containing the remaining mass of the removed homogeneous sphere (the cyan, blue, and red curves, respectively). We assume the void to be either co-expanding, the dashed curves ($\Delta\mathcal{T}$ is produced entirely by the time-delay contribution of Eq. (13)) or evolving according to linear perturbation theory, the solid curves ($\Delta\mathcal{T}$ is produced by the sum of Eqs. (13) and (14) with appropriate values for $d \log \delta / dz_d$, see Fig. 3).

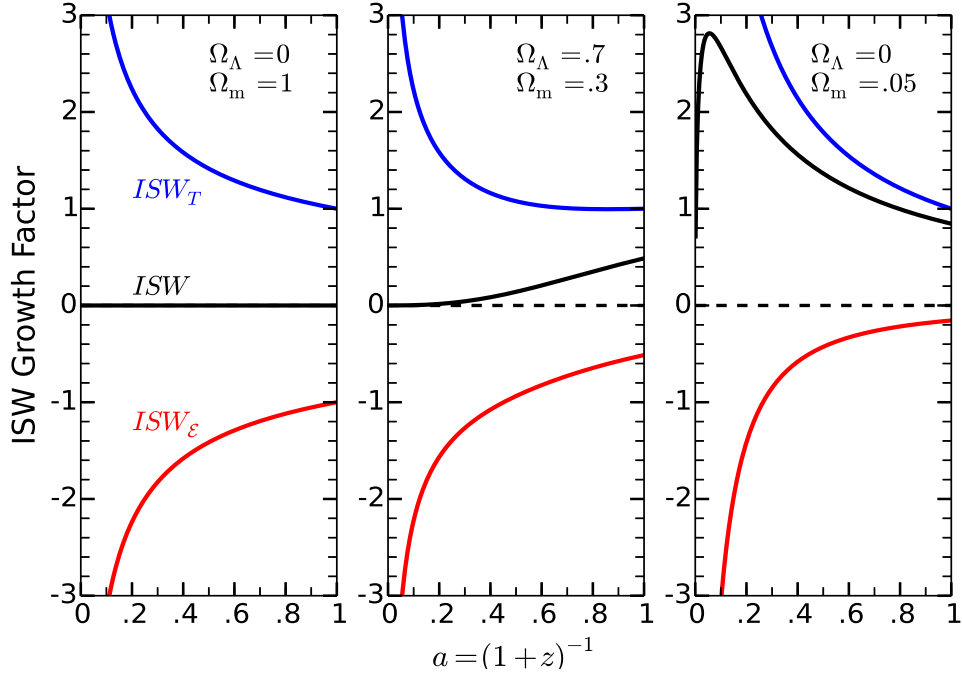


Fig. 3.— Redshift dependence of the ISW effect for the void models described in Section 3. We have tested three background FLRW cosmologies: EdS, concordance Λ CDM, and an open baryonic-matter only universe. The three curves in each panel correspond to the time delay contribution $\Delta\mathcal{T}_T(z)$, evolutionary contribution $\Delta\mathcal{T}_E(z)$, and the sum $\Delta\mathcal{T} = \Delta\mathcal{T}_T + \Delta\mathcal{T}_E$ (the blue, red, and black curves, respectively). All curves are normalized by $\Delta\mathcal{T}_T(z=0)$ for the corresponding cosmology. We have assumed a linear perturbation growth of voids when computing $\Delta\mathcal{T}_E(z)$ and $\Delta\mathcal{T}(z)$, see Eqs. (13) and (14).

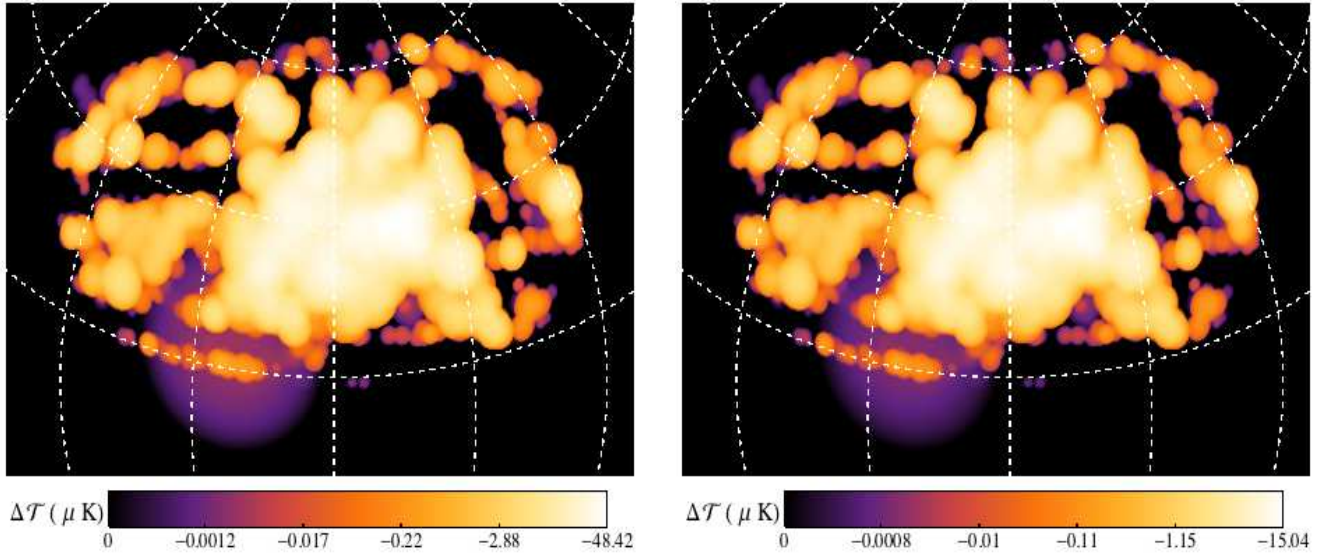


Fig. 4.— The Lambert equal-area projection of the sky map of CMB temperature fluctuations caused by passing through voids along the line of sight. We used the “central void catalog” (version 2014.06.18) of Sutter et al. (2012). The map is centered at RA = 180° and DEC = 30° with longitude and latitude lines separated by 30°. We use the same void model as in the right panel of Fig. 2 (the blue curves in the middle panel). For each void, we estimate its mass (or Schwarzschild radius r_s) using its effective radius and redshift provided by Sutter et al. (2012), we then compute $\Delta\mathcal{T}$ across this void using Eq. (13) assuming $\delta = -0.5$. For overlapping voids along a sight line, we add the $\Delta\mathcal{T}$ caused by each void. For the left panel, we assume the voids are co-expanding with the background Universe and only the time delay contributes. For the right panel, we assume a linear perturbation theory (see Fig. 3). Assuming a different void density contrast will also result in a similar figure except for a pure rescaling of the color-bar. For example, if we chose $\delta = -0.1$ instead of $\delta = -0.5$, then the signal will be reduced to one fifth of its current values for both scenarios.